A&A 544, A134 (2012)
DOI: 10.1051/0004-6361/201219288


Astronomy & Astrophysics

# VLT imaging of the $\beta$ Pictoris gas disk⋆

R. Nilsson[1], A. Brandeker[1], G. Olofsson[1], K. Fathi[1], Ph. Thébault[2], and R. Liseau[3]

[1] Department of Astronomy, Stockholm University, AlbaNova University Center, Roslagstullsbacken 21, 106 91 Stockholm, Sweden
e-mail: [ricky;alexis;olofsson;kambiz]@astro.su.se
[2] Observatoire de Paris, Section de Meudon, 92195 Meudon Principal Cedex, France
e-mail: philippe.thebault@obspm.fr
[3] Onsala Space Observatory, Chalmers University of Technology, 439 92 Onsala, Sweden
e-mail: rene.liseau@chalmers.se

Received 26 March 2012 / Accepted 3 July 2012

**ABSTRACT**

*Context.* Circumstellar debris disks older than a few Myr should be largely devoid of primordial gas remaining from the protoplanetary disk phase. Tracing the origin of observed atomic gas in Keplerian rotation in the edge-on debris disk surrounding the ∼12 Myr old star $\beta$ Pictoris requires more detailed information about its spatial distribution than has previously been acquired by limited slit spectroscopy. Especially indications of asymmetries and presence of Ca II gas at high disk latitudes call for additional investigation to exclude or confirm its connection to observed dust structures or suggested cometary bodies on inclined eccentric orbits.
*Aims.* We set out to recover a complete image of the Fe I and Ca II gas emission around $\beta$ Pic by spatially resolved, high-resolution spectroscopic observations to better understand the morphology and origin of the gaseous disk component.
*Methods.* The multiple fiber facility FLAMES/GIRAFFE at the Very Large Telescope (VLT), with the large integral-field-unit ARGUS, was used to obtain spatially resolved optical spectra (from 385.9 to 404.8 nm) in four regions covering the northeast and southwest side of the disk. Emission lines from Fe I (at 386.0 nm) and Ca II (at 393.4 and 396.8 nm) were mapped and could be used to fit a parametric function for the disk gas distribution, using a gas-ionisation code for gas-poor debris disks.
*Results.* Both Fe I and Ca II emission are clearly detected, with the former dominating along the disk midplane, and the latter revealing vertically more extended gas. The surface intensity of the Fe I emission is lower but more extended in the northeast (reaching the 210 AU limit of our observations) than in the southwest, while Ca II shows the opposite asymmetry. The modelled Fe gas disk profile shows a linear increase in scale height with radius, and a vertical profile that suggests dynamical interaction with the dust. We also qualitatively demonstrate that the Ca II emission profile can be explained by optical thickness in the disk midplane, and does not require Ca to be spatially separated from Fe.

**Key words.** circumstellar matter – stars: individual: $\beta$ Pictoris – planetary systems – techniques: imaging spectroscopy

## 1. Introduction

The transformation of dusty and gaseous disks around young stars into planetary systems involves a gradual clearing of the disk by several processes. Dense and gas-rich protoplanetary envelopes are affected by strong stellar radiation (Gorti & Hollenbach 2009) and winds (Lovelace et al. 2008), that compete with viscous accretion (Lynden-Bell & Pringle 1974) to open up growing inner disk holes, and cause complete photoevaporation of the gaseous disk component within ∼10 Myr (Zuckerman et al. 1995; Haisch et al. 2001; Jayawardhana et al. 2006; Pascucci et al. 2006). This also sets the time frame for giant planet formation, because it restricts the amount of gas available to be swept up by growing planetary embryos. Primordial dust grains are blown out from the system or spiral onto the star due to Poynting-Robertson (PR) drag and are cleared from the disk within a few thousand years. The left-over debris disk is defined by a low (<10%) gas-to-dust ratio, is mostly optically thin, and often observable as excess mid- and far-infrared (IR) emission in the spectral energy distribution (SED), originating from heated dust grains that are being continuously produced in collisions between planetesimals (Dominik & Decin 2003; Wyatt et al. 2007). Decrease in this steady-state collisional processing and continous removal of submicron sized dust by radiation pressure leads to a decline in observed IR excess with time. Most of the dust in a standard debris disk is believed to be composed of porous silicate grains containing Si, Mg, and Fe, likely combined with oxygen into forsterite ($Mg_2SiO_4$), enstatite ($MgSiO_3$), olivine ([Mg, Fe]$_2SiO_4$), and pyroxenes ([Mg, Fe]$SiO_3$), as found in chondritic meteorites (see review by Henning 2010). Beyond the ice condensation (snow) line, grains would contain a cometary fraction of $H_2O$, $CO_2$, CO, $NH_3$, $CH_4$, and $N_2$ ices, although there is a possibility that photo-sputtering might strip grains from their ices beyond the snowline (Grigorieva et al. 2007).

Observation of gas in such evolved non-primordial disks is not expected a priori. It is of course routinely observed in younger systems in the protoplanetary-disk stage. As an example, abundant molecular species (e.g. CO and $H_2$) in young circumstellar disks have been detected in both emission (Najita et al. 2003; Herczeg et al. 2006) and absorption (Redfield 2007; Roberge & Weinberger 2008). However, in most disk environments, especially around early-type stars, molecules like $H_2O$, OH, and CO are not expected to survive, instead producing an abundance of atomic oxygen and carbon by photodissociation

⋆ Based on observations made with ESO Telescopes at the La Silla Paranal Observatory under programme IDs 382.C-0394 and 384.C-0551.

(e.g. Kamp & Bertoldi 2000). Elements with strong resonant transitions in the ultraviolet (UV) and optical, especially metals, are then easily blown out from the system by radiation pressure. Thus, the detection of substantial quantities of gas in older systems that have presumably made the transition to debris disks, like the 30 Myr-old HD 21997 (Moór et al. 2011) and 200 Myr-old $\sigma$ Her (Chen & Jura 2003), is surprising and points to unknown gas retention or production mechanisms. If gas is being produced, it can give us information on the composition of solid bodies in the disk, and even small amounts of gas can affect the dynamics of dust grains (Thébault & Augereau 2005; Krivov et al. 2009). $\beta$ Pictoris is the only currently known debris disk that contains gas and is close enough to be spatially resolved at optical and IR wavelengths, allowing detection of resonantly scattered light and thus a more detailed study of gas composition and distribution.

The first indication of circumstellar material around the ~12 Myr A6V star $\beta$ Pic came from detection of thermal IR excess by the Infrared Astronomical Satellite (IRAS, Aumann 1985), and subsequent ground-based coronagraphic imaging revealed a flared, nearly edge-on dust disk in scattered optical and near-IR light (Smith & Terrile 1984; Paresce & Burrows 1987), extending out to 1800 AU. Following its classification as a debris disk star (or so-called Vega-like star, from the prototype IR excess star Vega, Backman & Paresce 1993), $\beta$ Pic has been extensively studied and the minimum mass of cold dust contained within its disk determined from submillimeter (submm) and millimeter observations to 3−10 lunar masses (Zuckerman & Becklin 1993; Holland et al. 1998; Dent et al. 2000; Liseau et al. 2003; Nilsson et al. 2009). In addition to the collisionally produced dust (Backman & Paresce 1993; Artymowicz 1997; Lagrange et al. 2000; Zuckerman 2001), several lines of evidence suggest that evaporating comets on eccentric orbits, so-called *falling evaporating bodies*, FEBs, are supplying dust to the $\beta$ Pic debris disk (Lecavelier Des Etangs et al. 1996, 1998). One comes from spectroscopic signatures of intermittent redshifted absorption lines (Lagrange-Henri et al. 1988; Beust et al. 1990; Vidal-Madjar et al. 1994, and references therein) and a second from emission by crystalline silicates (at 9.7, 28, and 33.5 $\mu$m) and olivines (at 11.3 $\mu$m) (Telesco & Knacke 1991; Knacke et al. 1993; Aitken et al. 1993; Weinberger et al. 2003; Okamoto et al. 2004; Chen et al. 2007), similar to that observed in e.g. comet Halley. This points to a cometary-like grain composition of either crystalline olivine (~55%), pyroxene (~35%), and other silicates, or a mix of 95% amorphous and 5% crystalline olivine (Artymowicz 1997, and references therein). Dissimilarities between disk features in IR emission and scattered light images of the disk imply that two distinctly different grain populations contribute, perhaps low-albedo refractory grains (like the hot, >300 K, silicates that are unmistakably responsible for the 10 $\mu$m emission) and high-albedo icy grains.

Information about the spatial distribution of circumstellar gas is more limited than the dust, since it is more difficult to observe. Several species of atomic gas have been detected in absorption, due to the disk's favorable edge-on orientation. The strong circumstellar Ca II K absorption line, e.g., was detected early, together with weaker Na I D lines (Vidal-Madjar et al. 1986; Hobbs et al. 1985), and several neutral and singly ionised metallic species have been observed in both optical and UV absorption spectroscopy (Lagrange et al. 1998). Surprisingly, these appear to be very stable (apart from the intermittent redshifted components) and do not show any radial velocity, which would be expected from acceleration by radiation pressure.

Olofsson et al. (2001) performed high-resolution slit spectroscopy along the disk of $\beta$ Pic and made the first spatially resolved detection of circumstellar atomic gas around any star. The Na I D emission line (doublet) at 5895 Å was found to be resonantly scattered from 30 to 140 AU, with an average Na I column density of $10^{15}$ cm$^{-2}$ and a velocity pattern clearly indicating gas in Keplerian rotation. To explain the absence of any detected radial motion – considering the fact that the force from radiation pressure felt by Na I throughout the $\beta$ Pic disk is 250 times stronger than the gravitational force – Olofsson et al. (2001) proposed fast ionisation by the intense stellar UV radiation, which does not allow significant time for acceleration of neutral Na I before conversion to Na II ions (which lack strong transitions in the wavelength region dominating the stellar SED). This model was recently improved by Brandeker (2011). In VLT/UVES observations over a wider spectral range and with a spatial and spectral resolution twice as high, Brandeker et al. (2004) detected 88 emission lines originating from Fe I, Na I, Ca II, Ni I, Ni II, Ti I, Ti II, Cr I, and Cr II. Spatial information from the slit placed at four positions across the disk (at 60 and 120 AU, on either side) and four positions along the disk revealed a surprisingly extended and asymmetric gas distribution. The strong Fe I and Na I emission reaches along the disk from 13 out to 323 AU from the star, displaying a NE-SW asymmetry similar to that observed in the dust, with a gradual NE radial decline and a sharp cutoff in the brighter (out to 75 AU) SW emission at 150−200 AU. Also in accordance with dust observations, an inner 5° tilt was found by Brandeker et al. (2004). The radial thickness increase of the gas disk appears to be significantly higher than that of the dust (almost twice the scale-height of the dust disk at 116 AU). Ca II H- and K emission can be traced to heights of 77 AU above the mid-plane, but falls off closer to the mid-plane. As in the observations by Olofsson et al. (2001), the outward radial motion of gas is much slower than would be expected from acceleration due to radiation pressure. This points to a braking agent that cannot be H I and $H_2$, which have observational upper limits in column density inconsistent with observed velocities, or perhaps an unknown gas production mechanism (Brandeker et al. 2004). Fernández et al. (2006) studied gas braking and production processes, concluding that deceleration of ions through Coulomb interaction with other ions (self-braking) could be sufficient to brake the gas, but only if C in the disk gas is at least five times overabundant compared to solar elemental abundances. Spectroscopic observations with the Far Ultraviolet Spectroscopic Explorer (FUSE) (Roberge et al. 2006) did find C II and C III measured in absorption to be significantly more abundant compared to elemental abundances of solar system material (viz. the Sun, carbonaceous chondrites, and dust from comet Halley), and could thus partly solve the radial velocity conundrum. More detailed modelling of the braking by Brandeker (2011) and observations by the PACS instrument at the *Herschel* Space Observatory (Brandeker et al. 2012) indicated that the C abundance over metallic elements such as Na and Fe might be even higher, of about 400× solar abundance.

Because of gas-removal mechanisms, the gas is probably not primordial (Fernández et al. 2006), but replenished. Suggested mechanisms include (1) gas released from star-grazing comets (Beust & Valiron 2007), (2) photo-desorption from circumstellar dust grains (Chen et al. 2007), and (3) vaporisation of dust by collisions with high-velocity $\beta$-meteoroids (Czechowski & Mann 2007). Since these different mechanisms should produce different spatial distributions of gas, one way to potentially distinguish between them is to map the spatial distribution of gas, which is the aim of this study. One would, e.g., expect most of

the gas released by comets to come from the inner regions of the system; the photo-desorption release of gas would be expected to be $\propto A(r)/r^2$, where $r$ is the distance to the star and $A(r)$ is the dust area density (since the UV radiation responsible for photo-desorption drops as $r^2$); while the dust-dust collision gas production profile would need more detailed modelling (as shown by Czechowski & Mann 2007). Once produced, the gas may get distributed/removed, which is another effect that needs to be taken into account to properly predict the current spatial distribution of gas. This detailed modelling is beyond the scope of the present paper, however, which focuses on the observed gas profile.

To obtain a complete map of the Fe I (at 386.0 nm) and Ca II (at 393.4 and 396.8 nm) emission throughout the disk of $\beta$ Pic, we used high-resolution integral field spectroscopy to cover the disk (Sects. 2 and 3). The observed emission from Fe I is modelled to obtain the spatial number density distribution of gas, combining a de-projection technique (Sect. 4.1) with the ionisation and thermal equilibrium code ONTARIO (Sect. 4.2). The obtained gas distribution is then used to compute the expected shape of the Ca II H emission profile, using a simple radiative transfer code to handle the optically thick H line (Sect. 5.1). Our conclusions are summarised in Sect. 6.

## 2. Observations and data reduction

### 2.1. Observations with FLAMES/GIRAFFE at VLT

The multi-object fiber facility FLAMES at the 8.2-m diameter Kueyen (UT2) telescope of the Very Large Telescope (VLT) array was used to obtain spatially resolved, high spectral resolution optical data of the $\beta$ Pic disk, employing its GIRAFFE spectrograph with the ARGUS fiber configuration. ARGUS is a large integral-field-unit (IFU) composed of a rectangular array of 22 × 14 microlenses, sampling either 0.52″/microlens (with a total sky coverage of 11.5″ × 7.3″) or 0.30″/microlens (6.6″ × 4.2″), and feeding the spectrograph through individual fibers. The high-resolution (HR) dispersion grating (with $R \approx 31\,300$ or $\mathrm{d}\lambda \approx 0.0126$ nm) offers a total spectral range of 370−950 nm accessed through various setups. We used the bluest HR setting with the central wavelength of the GIRAFFE grating at 395.8 nm. Observations were carried out in service mode, spread out over a period ranging from November 2008 to January 2010 (due to stringent $\lesssim$0.5″ seeing requirements), with an average airmass of 1.17. The ARGUS array was placed at four positions orthogonally along the disk (two on each side of the star), partially overlapping the smaller scale image of the inner disk with the larger scale image of the outer disk (as displayed in Fig. 1) to check for consistency. At each position, exposures were taken at two position angles (rotated 180°) to reduce the risk of having any sky areas repeatedly falling on dead pixels. Table 1 presents observing dates, field centre positions, position angles (PA), pixel scales, and exposure times of the observations.

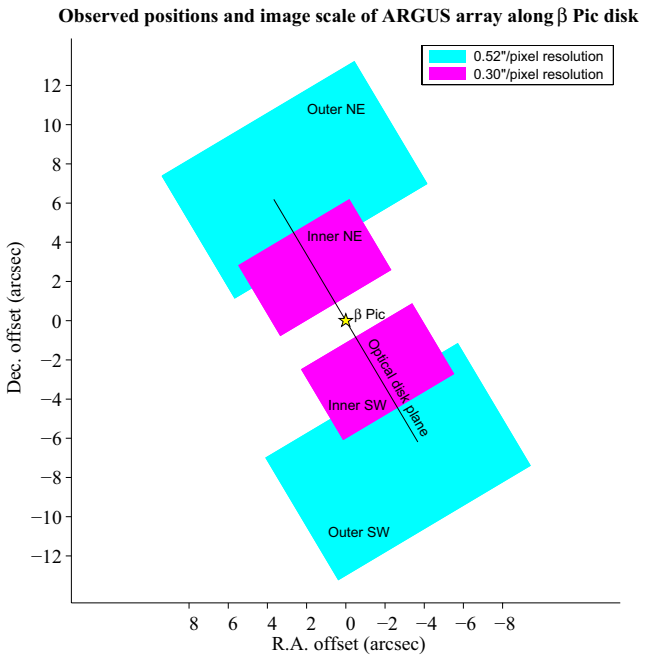


**Fig. 1.** Scale and position in the sky of the ARGUS array during the observations. The northeast (NE) and southwest (SW) side of the optical disk plane (marked with a black line) was covered, omitting the area closest to the star, where the stellar PSF and scattered light would be strong, giving low signal-to-noise ratio. Cyan- and magenta-coloured areas represent the higher (0.30″/pixel) and lower (0.52″/pixel) spatial resolution settings used for the inner and outer disk, respectively.

**Table 1.** log from VLT/FLAMES/GIRAFFE observations of $\beta$ Pic.

| RJD | RA[a] (°) | Dec[a] (°) | PA (°) | Scale (″/pix) | Exp. time (s) |
|---|---|---|---|---|---|
| 54774.72 | 86.8219 | −51.0656 | 300.75 | 0.30 | 895.0 |
| 54774.73 | 86.8219 | −51.0656 | 300.75 | 0.30 | 895.0 |
| 54774.75 | 86.8219 | −51.0656 | 300.75 | 0.30 | 895.0 |
| 54774.82 | 86.8219 | −51.0656 | 120.75 | 0.30 | 895.0 |
| 54774.83 | 86.8219 | −51.0656 | 120.75 | 0.30 | 895.0 |
| 54774.84 | 86.8219 | −51.0656 | 120.75 | 0.30 | 895.0 |
| 54798.70 | 86.8205 | −51.0670 | 300.75 | 0.30 | 895.0 |
| 54798.71 | 86.8205 | −51.0670 | 300.75 | 0.30 | 895.0 |
| 54798.72 | 86.8205 | −51.0670 | 300.75 | 0.30 | 895.0 |
| 54799.69 | 86.8205 | −51.0670 | 120.75 | 0.30 | 895.0 |
| 54799.70 | 86.8205 | −51.0670 | 120.75 | 0.30 | 895.0 |
| 54799.71 | 86.8205 | −51.0670 | 120.75 | 0.30 | 895.0 |
| 54912.50 | 86.8224 | −51.0643 | 300.75 | 0.52 | 2775.0 |
| 54913.51 | 86.8224 | −51.0643 | 120.75 | 0.52 | 2775.0 |
| 55193.70 | 86.8200 | −51.0683 | 120.75 | 0.52 | 2775.0 |
| 55225.65 | 86.8200 | −51.0683 | 300.75 | 0.52 | 2775.0 |
| 55225.70 | 86.8224 | −51.0643 | 120.75 | 0.52 | 2775.0 |

**Notes.** The optical coordinates of the star are RA = $05^{\mathrm{h}}47^{\mathrm{m}}17.088^{\mathrm{s}}$ and Dec = −51°03′59.44″ (J2000). [(a)] ARGUS field centre position.

### 2.2. Reducing FLAMES/GIRAFFE data

The raw images containing dispersed spectra from all fibers (including sky- and simultaneous calibration exposures) were reduced using ESO's recipe execution tool *EsoRex* with supplied GIRAFFE pipeline recipes. Calibration products (master bias, master flat-field with fiber localisation data, dispersion solution and line identification from simultaneous ThAr arc lamp spectra, and instrument response from standard star observations) were created and then applied in the reduction of science frames to retrieve flux- and wavelength-corrected spectra in each pixel of the reconstructed image. The final spectra were extracted by summing up over all pixels in the fiber width and were subsequently rebinned to a linear scale of 0.005 nm spectral elements (from the raw ∼0.0046 nm/pixel non-linear scale), ranging from 385.9 nm to 404.8 nm, with a measured average resolution (from ThAr lines) full-width at half-maximum (FWHM) of 0.0111 nm. Line-flux errors were estimated from the noise in the region surrounding each line, but it should be noted that the absolute photometric accuracy of the instrument response at

**Table 2.** Observed emission lines.

| Line | $\lambda_{air}$ (nm) | $E_j \rightarrow E_i$ (eV) | $A_{ji}$ $s^{-1}$ | $g_j - g_i$ |
|---|---|---|---|---|
| Fe I | 385.99114 | 3.211→0.000 | $9.69 \times 10^6$ | 9–9 |
| Ca II K | 393.36614 | 3.151→0.000 | $1.47 \times 10^8$ | 2–4 |
| Ca II H | 396.84673 | 3.123→0.000 | $1.4 \times 10^8$ | 2–2 |

**Notes.** Data retrieved from NIST (http://physics.nist.gov).

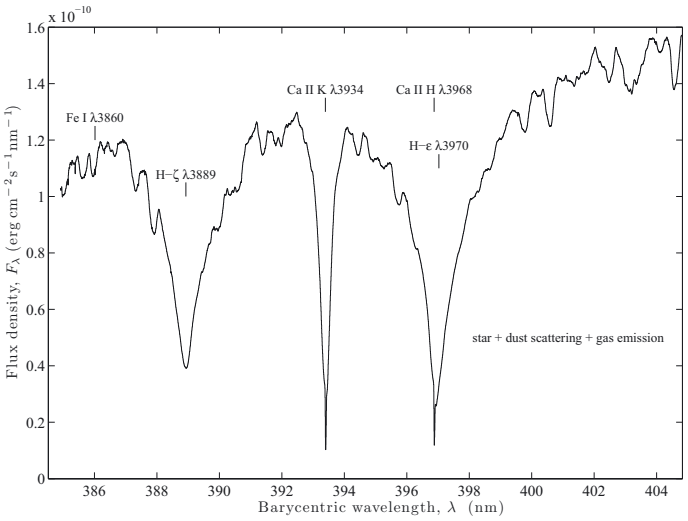


**Fig. 2.** Total observed near-UV spectra of inner disk, comprised mainly of a stellar PSF component, with additions from gas emission and light scattered off circumstellar dust grains.

these blue wavelengths are not better than ~20%, judging from the standard deviation of obtained instrument response curves (see Fig. A.1 in Appendix A).

The data cubes were further processed in MATLAB, where barycentric wavelength correction and airmass correction was applied, and images were combined. Most cosmic ray hits could be identified and eliminated by sigma clipping and vertical (spectral dimension) interpolation directly in the unprocessed images. Remaining spikes in the spectra of the inner disk could be removed by modified median filtering, replacing values in the contaminated spectrum with the mean of the two additional exposures obtained (after normalisation), but the long single exposures of the outer disk presented a bigger problem. In that region we had to replace identified spikes with values interpolated from neighbouring bins, taking care to correct for occasional adjacent or extraordinarily wide spikes by comparing with the rotated exposure. The fact that the unresolved emission lines we were mapping had a width comparable to the average width of the cosmic ray spikes added to the complication.

### 2.3. Isolating the emission lines

To extract the flux from the Fe I and Ca II emission lines (Table 2) we had to subtract the dominant stellar point-spread function (PSF) and dust-scattered light contribution to the total spectrum (Fig. 2).

A spectrum (with FWHM resolution ~0.004 nm and sampling of 0.001 nm/pixel) of $\beta$ Pic showing no signs of FEBs, which had previously been obtained from the HARPS spectrograph at the ESO 3.6-m telescope, was convolved with a Gaussian of $FWHM = 0.0111$ nm (measured average resolution from arc spectra) and rebinned to 0.005 nm, and used as a reference stellar spectrum, $f_\star$. This was then fitted to the observed spectrum, $f_{tot}$, surrounding each emission line region and in each pixel individually by unconstrained non-linear minimisation of the function

$$f_{disk}(\lambda) = f_{tot}(\lambda) - \left(k_1\lambda^2 + k_2\lambda + k_3\right) f_\star(\lambda) - k_4, \quad (1)$$

essentially multiplying it with a second-degree polynomial (which was interpolated across the line), but with compensation for offset level. This baseline was then subtracted to recover the gas emission lines. For the inner disk observations of Ca II we substituted the HARPS spectrum with a stellar spectrum derived from the mean of eight off-disk pixels with strong stellar PSF contribution, since redshifted Ca II components from FEBs were visible in these epochs. The total line flux was found by integrating the spectral energy distribution over the approximated line width at the central wavelength position of the Doppler shifted line (assuming Keplerian rotation of the gas disk). These steps involved some tweaking of parameters (e.g. regions for baseline-fit and interpolation, and fitting function) to minimise the effects from noise and certain spectral features. Specifically, the Ca II H- and K emission lines are superimposed onto the broad stellar and narrow circumstellar Ca II H- and K absorption lines, making the fit of the stellar spectrum very sensitive to the chosen fitting region, and consequently affecting the subtracted baseline. Although this overlap made the reduction more difficult, it also helped by suppressing the background PSF noise of the Ca II emission. Figure 3 shows emission lines of Fe I and Ca II H and K in two selected pixels, together with fitted baselines and regions used in the extraction. The baseline fitting regions extend 100 and 500 wavelength bins on either side of the emission lines for Fe I and Ca II, respectively. The position of the line peaks coincides with expected Doppler-shifts due to Keplerian rotation relative to the systemic velocity of $\beta$ Pic. Apparent redshifted offsets from systemic velocity in the Ca II H- and K *absorption* is a clear indication of the presence of FEBs.

The signal-to-noise ratio (S/N) of the emission lines was estimated by dividing the baseline-subtracted peak flux with the standard deviation, $\sigma$, of the surrounding spectral region.

## 3. Results

### 3.1. Disk seen in gas emission

Resulting maps of Fe I λ3860 and Ca II H- and K emission in the disk of $\beta$ Pic are presented in Figs. 4–6, where the (b) panels display the intensity scaled with projected distance to the star squared to bring out detail in the outer regions. The optical dust-disk midplane is marked by a blue line, and the tilted 4.5° secondary disk with a cyan-coloured line. Fe I λ3860 emission is clearly visible along the disk midplane, while Ca II H- and K emission is strongest in higher latitude areas on the NE and SW side. Both exhibit a highly asymmetric distribution; Fe I being fainter but more extended in the NE than in the SW, and Ca II showing the opposite behaviour, in addition to asymmetries relative to the disk midplane. Fe I is detected at disk radii out to the 210 AU limit of our observations in the NE, while Ca II appears to be reaching beyond the observed ~100 AU latitudes on the SW side. Data from the innermost 2–3 columns (~20–30 AU) are very noisy due to strong contamination by light from the stellar PSF, therefore it is hard to tell if there is a decline in flux inward of the peaks at ~40 AU. However, inspection of the maps normalised with distance squared suggests that

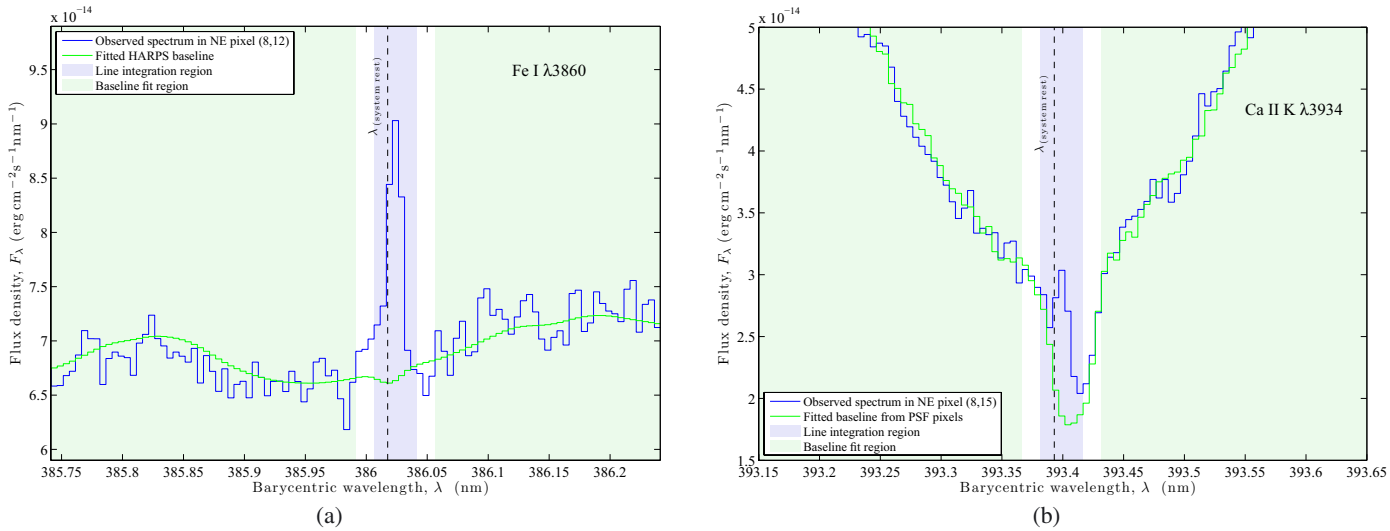


**Fig. 3.** Example spectra of Fe I λ3860 **a)** and Ca II K **b)**, both sampled from the NE side of the disk. The regions used for baseline fitting and line integration are indicated, as is the systemic rest velocity of $\beta$ Pic (dashed vertical line).

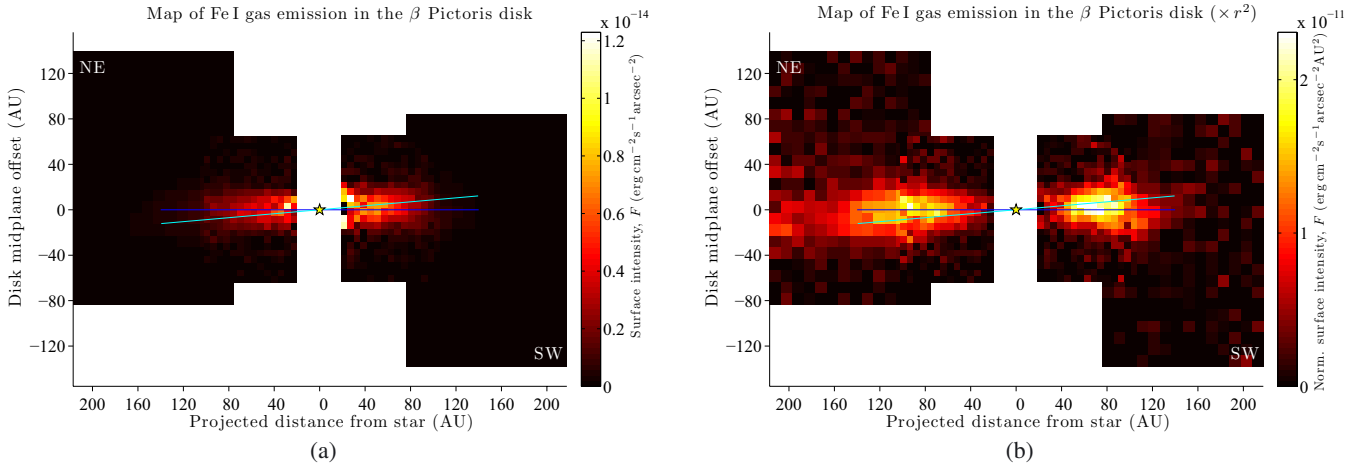


**Fig. 4.** Map of Fe I emission, multiplied with the projected distance to the star squared in panel **b)**. The blue line indicates the disk midplane (defined to be at 30.75°) while the green line shows the orientation of the inner disk, as found in dust disk observations.

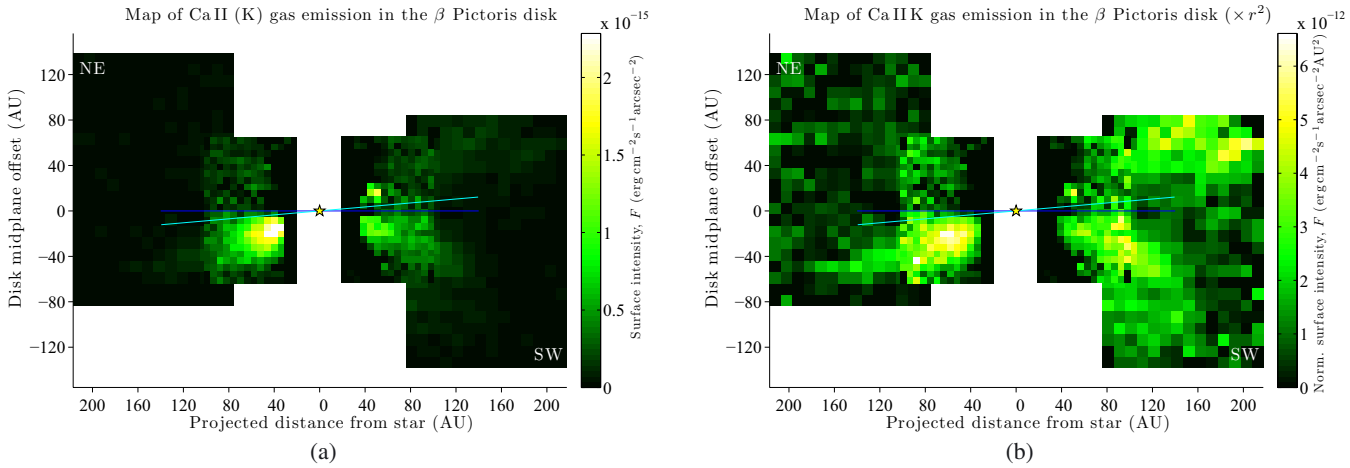


**Fig. 5.** As in Fig. 4, but for Ca II K.

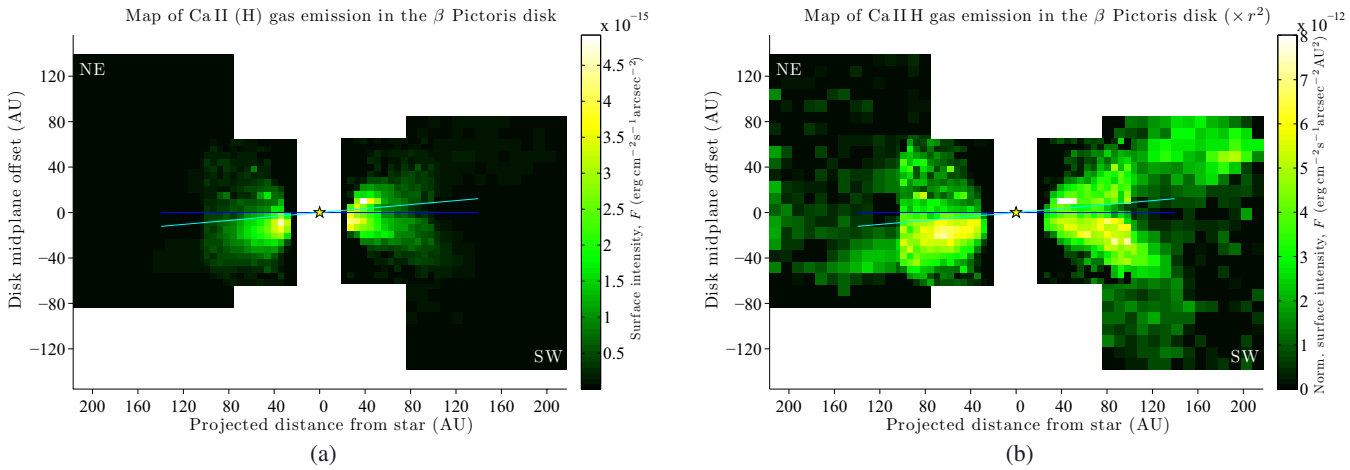


**Fig. 6.** As in Fig. 4, but for Ca II H.

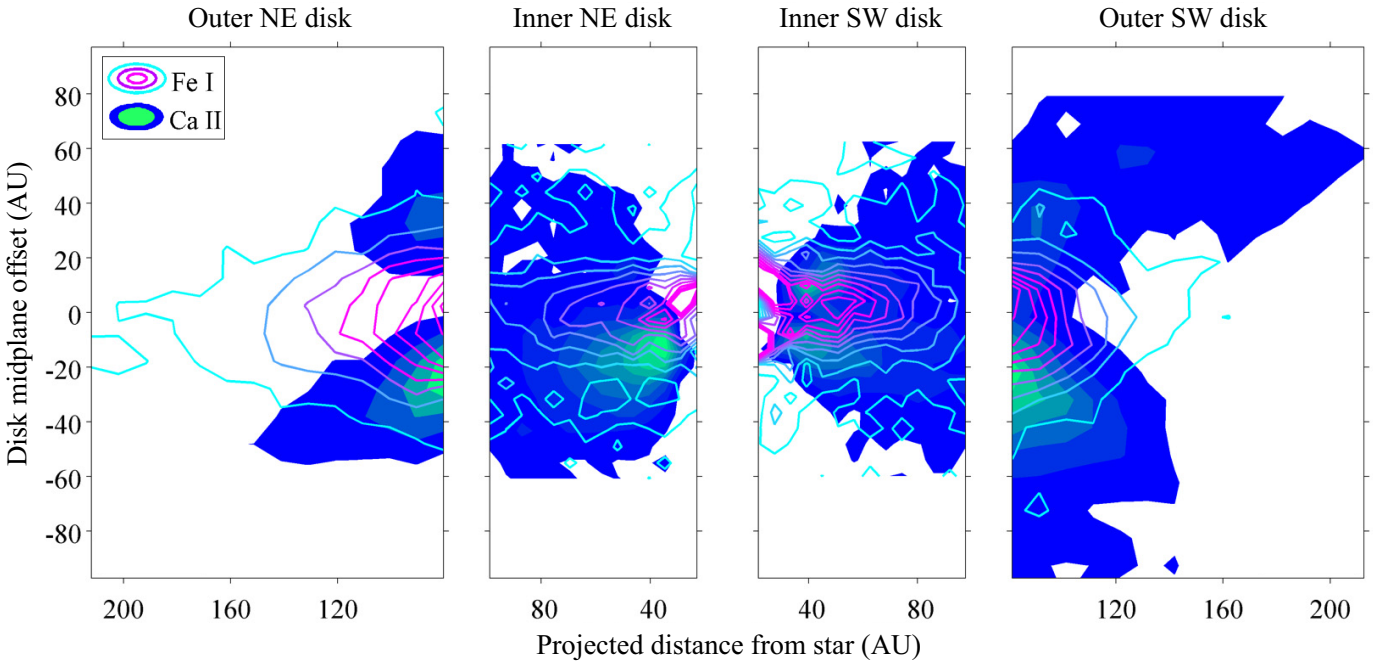


**Fig. 7.** Contour map of Fe I and Ca II H- and K emission. The contour levels of inner and outer panels differ and are just meant to give a clearer picture of the relative positions of dominant Fe I and Ca II emission regions.

there is a peak in the *column density* of Fe I at ~90 AU in the NE and ~70 AU in the SW. Because Ca II H- and K emission is optically thick, we cannot immediately draw similar conclusions for Ca II, as discussed in detail in Sect. 5.1.

A brightness difference can be observed in the overlapping regions between observations of the outer and inner disks. This can be caused by a number of factors and is discussed in more detail in Appendix A.

Figure 7 clearly shows how the emission contours from neutral Fe outlines the disk midplane, while singly ionised Ca emission appears weaker in that same region, instead dominating at high latitudes and increasing with radial distance, forming a characteristic butterfly shape. Note that this figure is only presented to highlight the relative positions of regions with dominating Fe I and Ca II gas emission, and that the contour levels of the inner and outer parts differ.

## 4. Analysis

Our primary interest is to find the spatial gas density distribution in the disk. The location of the gas gives clues to its origin, and can also put constraints on potential planet-disk interaction (as has indeed been done for the observed spatial *dust* distribution). Of particular interest is the Ca II observed at surprisingly high scale-heights above the disk midplane, and the possible mechanisms that may have placed the Ca there.

The problem of inverting observed flux into gas density is not trivial, because we are observing an essentially edge-on projection of the disk emission, where the emission at each projected distance is the contribution from many locations in the disk along the line of sight. If we furthermore consider the possibility of an asymmetric disk, the problem of finding the gas density distribution from the observed projected flux becomes degenerate. To break the degeneracy, we assumed that the disk is cylindrically symmetric. Since we observe significant

differences between the NE and SW sides of the disk, we know that this assumption is of limited validity; we therefore made independent inversions of the two sides to get an impression of the uncertainties involved. To simplify the procedure even more, we divided the problem into two steps:

1. De-project the Fe I λ3860 emission from the disk to obtain the spatial luminosity density as a function of cylindrical radius $r$ and height $z$ (assuming cylindrical symmetry).
2. Use the derived 2D luminosity density profile to derive the Fe gas density, with the help of the ionisation, thermal balance, and level population statistical equilibrium code ONTARIO.

The inversion from the Fe I λ3860 luminosity density to the number density of Fe is complicated by the complex energy level structure of Fe I. The level population is dominated by photo-excitation, hence the need for a non-LTE (local thermal equilibrium) solver (part of ONTARIO). Furthermore, the Fe I λ3860 emission is expected to be optically thin; for a line width of 1.5 km s$^{-1}$ (Crawford et al. 1994), the mid-plane column density of Fe I towards the star is $7 \times 10^{11}$ cm$^{-2}$ (Zagorovsky et al. 2010), and conservatively assuming *all* atoms to be in the ground state, the optical depth of the λ3860 transition becomes $\tau \sim 0.1$.

In contrast, assuming a solar abundance ratio of Fe/Ca (Zagorovsky et al. 2010), the Ca II H- and K lines are strongly optically thick ($\tau \sim 100$ in the mid plane). We therefore did not attempt to use the Ca II lines to derive the gas density of Ca, since even small deviations from cylindrical symmetry in density will give large variations in emitted flux, making the inversion strongly degenerate. Instead, we used the spatial gas distribution derived from Fe I, solved for the radiative transfer and computed the expected Ca II H- and K emission from the disk, in an attempt to check whether there is chemical segregation, as has been previously suggested (Beust & Valiron 2007).

In the following subsections, the inversion steps are outlined in detail.

### 4.1. Finding the Fe I λ3860 luminosity density profile

To find the de-projected luminosity density profile of Fe I λ3860, we assumed cylindrical symmetry and fitted a few-parametric functional form to the observed flux distribution. In line with Brandeker et al. (2004), we used a broken power-law for the radial dependence but introduced two new parameters for the height dependence ($\gamma$) and the scale-height dependence ($\delta$) on the midplane radius $r$:

$$L(r,z) = l_0 \left[ \frac{2}{(r/r_0)^{2\alpha} + (r/r_0)^{2\beta}} \right]^{1/2} \exp\left[ -\left( \frac{z}{h(r)} \right)^{\gamma} \right], \quad (2)$$

where $\alpha$ and $\beta$ are the parameters describing the shape of the power-law on either side of the inflection point $r_0$, and the vertical scale-height at each $r$ defined as

$$h(r) = h_0 \left( \frac{r}{r_0} \right)^{\delta}. \quad (3)$$

The parameter $\delta$ describes the "flaring" of the disk. For $\delta = 0$ we have a constant thickness disk, while for $\delta = 1$ the disk scale height increases linearly with radius. For $\delta > 1$ we have a flaring disk, i.e. the disk opening angle increases with radius. The parameter $\gamma$ determines how quickly the density drops with height. For a gas disk in thermostatic equilibrium we would expect the number density to drop as a Gaussian function, i.e. $\gamma = 2$. The dust distribution, on the other hand, is best fitted by closer to an exponential ($\gamma \approx 0.5$; Ahmic et al. 2009).

For a given set of parameters, $L(r,z)$ was projected onto a plane from edge-on to a resolution ten times better than the observations. The projected flux distribution was then convolved with the seeing recorded for the observation by using a Gaussian of the same FWHM, and re-sampled to the grid of the observations for comparison with observed data. By computing the residuals weighted by the noise, the best-fit values for the parameters $l_0$, $h_0$, $r_0$, $\alpha$, $\beta$, $\gamma$, and $\delta$ were found by $\chi^2$-minimisation. Figure 8 displays maps of observed Fe I emission, estimated noise, best-fit degraded model, and weighted squared residuals of the model fit. Resulting parameter values from fitting of the gas-disk profile and associated errors are presented in Table 3. The errors were estimated using the Monte-Carlo method to make repeated fits to the data with added noise drawn from the calculated noise distribution in each pixel.

### 4.2. Finding the gas density from the luminosity density

To find out how much gas we need to produce the inferred luminosity density of a Fe I λ3860, we have to answer these questions:

1. What is the number fraction of Fe in the gas?
2. What is the fraction of Fe in the neutral, atomic state?
3. What is the fraction of the Fe I that is radiating at λ3860?

Because $\beta$ Pic is an A-type star, we expect its radiation field to dissociate almost all molecules in its disk, leaving only atomic and ionised gas components. This simplifies the estimate of free Fe atoms because we can ignore chemical interactions, and only need to consider the ionisation state. For this we used the ONTARIO code (Zagorovsky et al. 2010), which self-consistently models the ionisation states and gas temperatures in debris disks around A- and F-type stars given a known stellar flux and gas/dust profile. It performs a full statistical equilibrium computation for several atomic species to find dominant absorption and emission lines. The local gas temperature is determined by the balance of heating and cooling mechanisms, and can, for the assumed optically thin gas, be treated in independent computation bins. The dominating heating processes for $\beta$ Pic are photoelectric heating by dust, and photoionisation of gas by stellar UV light, while cooling is dominated by fine-structure transitions (in particular from C II and O I, as recently detected in emission by the *Herschel* Space Observatory, Brandeker et al. 2012). A detailed description of the code can be found in Zagorovsky et al. (2010).

By iterating ONTARIO with different gas densities, the density that best reproduced the given emission for each grid cell was found. The abundance of elements in the gas was assumed to be solar (Grevesse & Sauval 1998), except for H (0.1% of solar), He (none), and C and O (400 times solar) as inferred from observations (Brandeker et al. 2012). The resulting gas profiles (separately for the NE and SW sides) are presented in Fig. 9 together with a best analytical fit, using the same parameters as $L(r,z)$ of Eq. (2) but with the luminosity density $l_0$ replaced by a number density $n_0$, which is a parameter that refers to the number density of H had it been at solar abundance. The number density of any given element can then be found by multiplying $n_0$ with the abundance relative to H (had H been at solar abundance). For instance, the number density of Fe is given by $n_{\rm Fe} = 2.8 \times 10^{-5} n_0$ and C by $n_{\rm C} = 9.8 \times 10^{-2} n_0$.

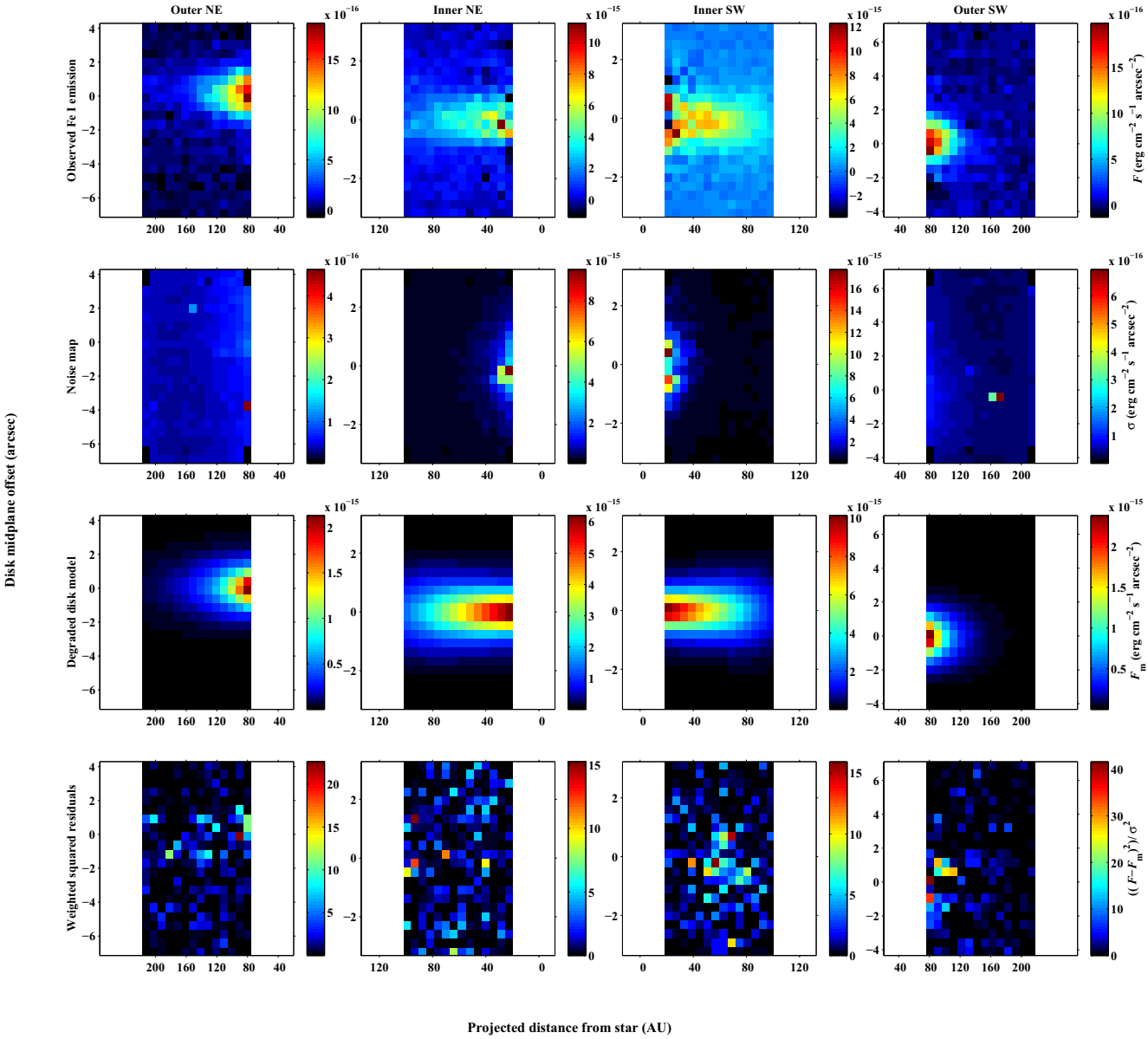


**Fig. 8.** Display of input data and results from $\chi^2$-minimisation disk-modelling of the Fe I emission. The rows of panels show, from the top down: observed Fe I emission maps, derived noise maps, degraded model maps, and maps of the weighted squared residuals. The reduced $\chi^2$ values are 1.9 (NE) and 2.3 (SW).

**Table 3.** Best-fit parameters and errors.

| | Fe I λ3860 luminosity | | | | Density | |
|---|---|---|---|---|---|---|
| | NE | | SW | | NE | SW |
| Parameter | value | $\sigma$ | value | $\sigma$ | value | value |
| $l_0$ ($10^{-19}$ erg s$^{-1}$ cm$^{-3}$) | 5.54 | 1.10 | 8.59 | 1.60 | – | – |
| $n_0$ ($10^3$ cm$^{-3}$) | – | – | – | – | 1.19 | 1.76 |
| $h_0$ (AU) | 16.4 | 1.0 | 16.9 | 1.0 | 21.8 | 20.4 |
| $r_0$ (AU) | 87.7 | 4.9 | 85.4 | 3.3 | 94.3 | 83.9 |
| $\alpha$ | 4.98 | 0.15 | 6.88 | 0.24 | 3.00 | 3.86 |
| $\beta$ | 1.15 | 0.28 | 1.38 | 0.29 | 0.83 | 0.93 |
| $\gamma$ | 1.50 | 0.11 | 1.57 | 0.11 | 1.26 | 1.33 |
| $\delta$ | 0.93 | 0.07 | 1.19 | 0.10 | 0.96 | 1.21 |

## 5. Discussion

Looking at the spatial distribution, we confirm the strong asymmetry between the NE and SW sides of the disk, where the SW gas density seemingly drops much quicker with radius at a rate $\propto r^{-3.9}$ compared to the NE side $\propto r^{-3.0}$. Neither side shows evidence for flaring, as $\delta \sim 1$. This means that the $h/r$ ratio is fairly constant and close to $h_0/r_0 \sim 0.2$. The height dependence with $\gamma \sim 1.3$ is closer to exponential ($\gamma = 1$) than the Gaussian ($\gamma = 2.0$) one would expect from hydrostatic equilibrium. This could be an indication that the gas dynamics is significantly affected by the dust grains, as found by Fernández et al. (2006) to be expected for an ionised gas interacting with charged dust.

### 5.1. The Ca II profile

In contrast to the detected Fe I emission (Fig. 4), the Ca II H- and K emission (Figs. 5, 6) is observed far away from the midplane. An interesting question is whether there is a mechanism preferentially transporting Ca to far heights above the midplane (as argued by e.g. Beust & Valiron 2007), or if there is another reason for Ca II emission to be preferentially emitted there. A significant difference between Ca II and Fe I (and the other spatially mapped species Na I from Brandeker et al. 2004) is that,

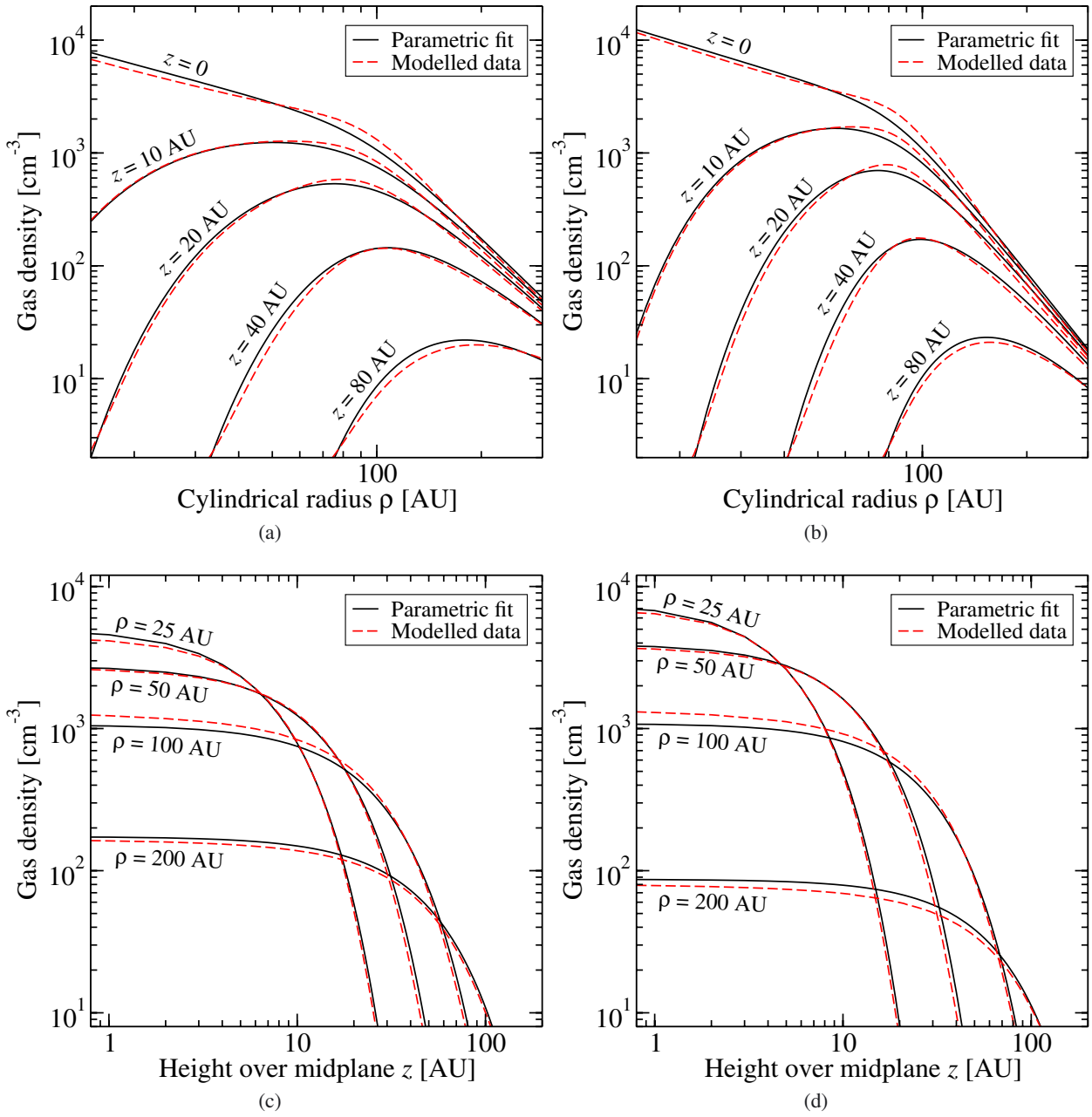


**Fig. 9.** Hydrogen-equivalent gas density inferred from Fe I λ3860 with parametric fits. Multiply with used abundance fraction to obtain the density of any specific element (well-mixed gas is assumed). NE to the *left* and SW to the *right*; *top panels* show cuts parallel to the midplane at heights $z$ above the plane and the *bottom panels* cuts orthogonal to the midplane at cylindrical radii $r$.

since the metals are all strongly ionised, the number density of Ca II is 15−500 times higher than the neutral Fe I (and Na I). Furthermore, the H- and K transition probabilities of Ca II are 10× higher. Together, this means that while the neutral transitions are optically thin, the Ca II lines are optically thick. A reason for the paucity of midplane emission could therefore be that the star is obscured by the gas, and that the only photons being scattered from the H- and K transitions in the midplane either come from secondary sources (e.g. photons scattered down from higher altitudes) or from far out in the wings, where the lines are still optically thin.

To test the idea that the optical properties are responsible for the difference in appearance between the Fe I λ3860 and Ca II H- and K emission maps, we implemented a simple radiative transfer code to compute the emerging emission map. Because we expect the lines to be optically thick, the line shape is important as the optical depth will vary over the line profile. Furthermore, because the gas is orbiting the star, there will be a velocity field that will Doppler-shift the line profile depending on the velocity projected on the line of sight. In detail, our model is based on the following assumptions and parameters:

1. The spatial distribution of gas is assumed to be the one in Table 3, inferred from the Fe I λ3860 emission (we assume different profiles for the NE and SW sides). The number density of Ca II is then computed using ONTARIO with the same parameters as used when inverting the Fe I emission profile.
2. For the velocity field, circular Keplerian orbits are assumed with a dynamical mass equal to $M_{\rm dyn} = 1.4\ M_{\odot}$ (Olofsson et al. 2001).

3. As an intrinsic line profile, a Voigt profile is assumed with broadening parameter $b = 1.5$ km s$^{-1}$. This is close to, but slightly below, the broadening parameter measured in absorption ($b = 2.0 \pm 0.7$ km s$^{-1}$; Crawford et al. 1994), which on the other hand probes the full column of gas along the midplane.
4. A 2D luminosity profile is computed, where the emission as a function of wavelength is derived as a function of cylindrical radius and height above the midplane. The luminosity profile Doppler-shifted by the projected velocity is then integrated through the disk for the line of sight, taking the (also Doppler-shifted) line opacity along the line of sight into account.
5. For the line scattering redistribution function we try three different cases:
   (a) Complete redistribution, that is, the outgoing photon is re-emitted at a wavelength with a probability according to the (Doppler-shifted) line profile, independent of the wavelength of the absorbed photon. This is a good approximation if the Ca II is disturbed (by a collision) before emitting again, which is likely not the case in the present circumstances because of the strength of the transition and the low density of gas.
   (b) Coherent scattering, that is, the re-emitted photon has exactly the same wavelength as the absorbed one (only Doppler-shifted). This is likely a better approximation, but essentially assumes that there is no Doppler-shift of the photons due to thermal motion, only the Keplerian velocity field.
   (c) Partially coherent redistribution, which assumes coherent scattering *in the rest frame of the scatterer*. Because of thermal motions, this implies a wavelength shift between the incoming and outgoing photon on top of the Keplerian velocity field. With the thermal motions isotropically and Maxwellian-distributed, the wavelength shift distribution will depend on the angle between the incoming and outgoing direction (Unno 1952). We take this into account by convolving the coherent line luminosity profile with the scattering function, which depends on the angle between the star, the volume element, and the observer. The thermal motions are assumed to correspond to the same broadening parameter $b = 1.5$ km s$^{-1}$ as before.

   To illustrate the differences between the three assumptions we plot a projected height emission profile in Fig. 10. Because complete redistribution brings photons in the line wings closer to the line centre (on average), it effectively creates higher optical depths and strongly suppresses the emerging flux from the midplane. For our fiducial model, we used partial redistribution.

The resulting Ca II H profile from the model (with partial redistribution) is shown in Fig. 11, which indeed shows the same characteristics as the observations: suppressed emission from the midplane and emission visible high above the plane. We emphasize that we used precisely the same spatial distribution of gas as was inferred from the optically Fe I λ3860 – we did not attempt to carefully fit the Ca II H emission. Still, the model reproduces the observations closely, but not perfectly. Since the model is symmetric with respect to the midplane, it does not show the strong asymmetries seen in the observations. Furthermore, the emission predicted by the model is about a factor 2−3 higher than seen in the observations. The discrepancies are not too surprising given that we assumed a spatial distribution of gas far

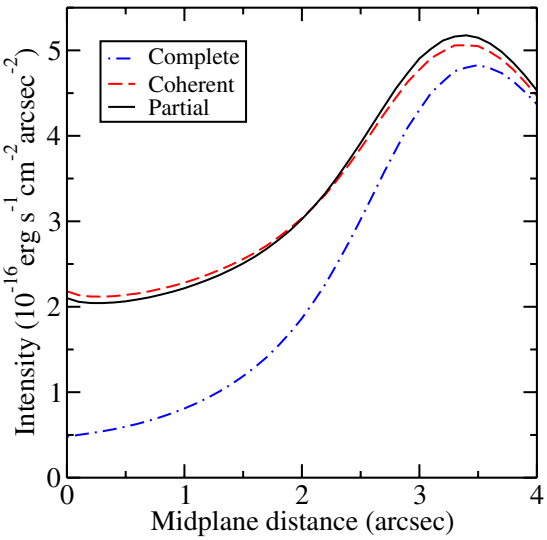


**Fig. 10.** Modelled Ca II H emission profile, using three different photon scattering redistribution functions. The figure shows a vertical cut at a distance of 120 AU at the SW side.

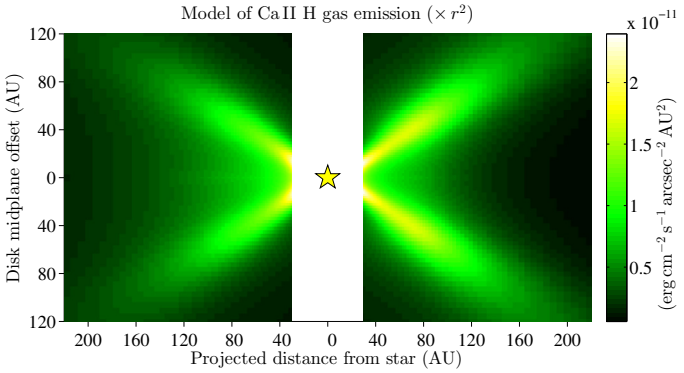


**Fig. 11.** Modelled Ca II H emission profile, assuming the gas distribution derived from Fe I λ3860.

beyond where it is well constrained by Fe I λ3860, e.g. both much higher above the midplane and closer in to the star than Fe I is detected. Small deviations in the Ca II density can make big differences in the Ca II H line luminosity. This could also explain why the Ca II emission extends farther into the SW than the NE, the opposite to what is observed for Fe I; it could simply be an optical depth effect, through which Ca II is shielded by a higher column density towards the star (while the Fe I is optically thin). Overall, however, we see no evidence that Fe and Ca are *not* well mixed; the striking difference between the observed intensity maps of Fe I λ3860 and Ca II H and K is well explained by the difference in optical depths between the lines.

### 5.2. Comparison between gas and dust profiles

The general NE/SW asymmetry of the gas disk is, as shown already by Brandeker et al. (2004), similar to that of the dust. Our parametric model of the gas number density profile can be compared to the parametric fits of the dust profile by Chen et al. (2007) and Ahmic et al. (2009) to assess how the gas-to-dust ratio varies as a function of disk radius (see Fig. 12). Outside the break radius the distribution of gas follows that of the dust model by Ahmic et al. (2009), while the results from Chen et al. (2007) indicate a faster decline of the dust number density.

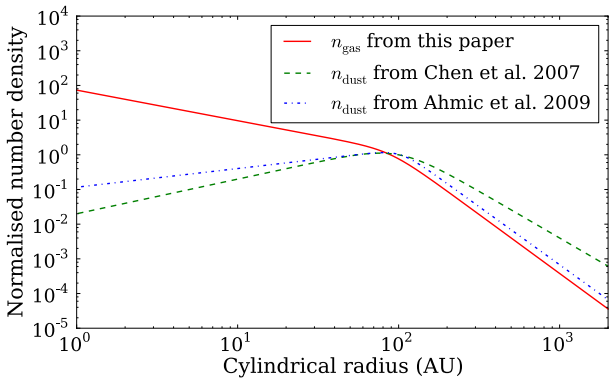


**Fig. 12.** Number density distribution of gas and dust in the $\beta$ Pic disk midplane, normalised to unity at the break radius, and shown for mean of parameters derived for NE and SW. We used the one-disk parametric fit from Ahmic et al. (2009).

Inside 100 AU the gas number density increases towards the star, in contrast to the dust. Interpreting the connection between the distributions of gas and dust requires more detailed modelling of gas production and redistribution, which is outside the scope of the current paper (see Xie et al. 2012, for a first attempt at relating disk properties to physical production/redistribution mechanisms).

## 6. Summary

Our main results are:

1. We have produced the first well-sampled *images* of the $\beta$ Pic gas disk and detected spatially resolved emission from Fe I and Ca II.
2. We confirm the NE/SW asymmetry previously found by Brandeker et al. (2004).
3. We find no evidence for flaring, i.e. the disk scale height increases linearly with midplane distance to the star.
4. The disk height profile drops slower than expected for a gas disk in hydrostatic equilibrium. We speculate that this might be caused by the dynamical interaction between ions and charged dust grains.
5. The Ca II H- and K spatial emission profiles indicate that Fe and Ca are well mixed throughout the disk; the difference to the Fe I $\lambda$3860 profile is caused by differences in optical depth.

*Acknowledgements.* The authors gratefully acknowledge financial contributions from Stockholm Astrobiology Graduate School, and the International Space Science Institute (ISSI) in Bern, Switzerland (Exozodiacal Dust Disks and Darwin working group, http://www.issibern.ch/teams/exodust/). A.B. was funded by the Swedish National Space Board (contract 84/08:1), while K.F. was funded by the Swedish Research Council. We would also like to thank Reinhard Hanuschik for clarifications regarding the EsoRex pipeline products.

## Appendix A: Flux calibration and comparison with UVES data

As mentioned in Sect. 2.2, the photometric accuracy of FLAMES/GIRAFFE/ARGUS depends to a great extent on the spectral response curve derived from observed standard stars. Unfortunately, the stellar models to which the standards are compared are very coarse in the blue spectral region observed, lacking any detailed spectral features. Moreover, the spectra are extracted by summing up over all pixels in the ARGUS array

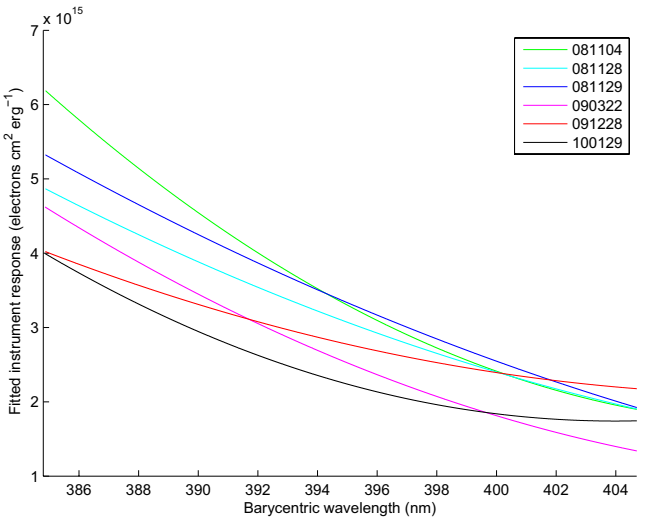


**Fig. A.1.** Fitted spectral instrument-response curves from observed standard stars, with colours marking observing dates.

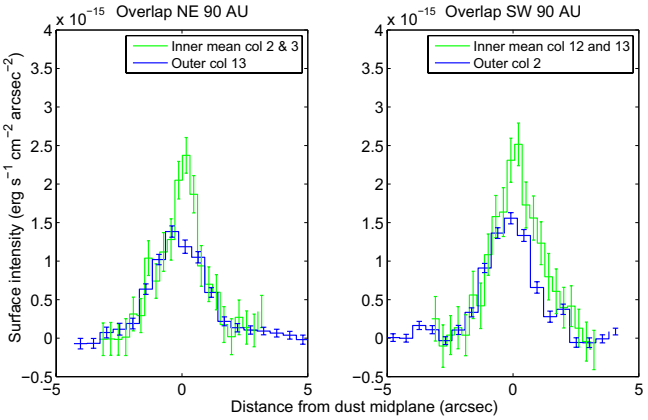


**Fig. A.2.** Comparison of Fe I emission in overlapping areas of inner and outer NE and SW observations. The pixel columns are counted from left to right in the four observed regions.

when running the *EsoRex* pipeline, adding sky emission and cosmic ray spikes. Owing to this, a reasonable spectral instrument-response curve has to be fitted to some well-chosen points in the noisy pipeline-derived instrument response before it can be applied to correct our observed target spectra. The fitted response curves from individual observing nights are presented in Fig. A.1. Such seemingly large differences in efficiency levels between different observations are unlikely, and must, at least partly, be attributed to photometric uncertainties in the GIRAFFE spectrograph. Observations of the same standard star at three different occasions (green, blue, and cyan lines), e.g., suggest a spectral instrument-response that varies by as much as 30% at the bluest wavelengths. Taking all these factors into account, we estimate a photometric accuracy of at best 20%.

To examine the relative accuracy of the flux calibration in more detail, we plotted the Fe I $\lambda$3860 and the Ca II H- and K signal in overlapping inner and outer observed FLAMES regions, as well as overlapping data obtained with UVES by Brandeker et al. (2004). The Fe I emission seems to be roughly consistent at higher latitudes in the inner/outer comparison, but there is a clear difference close to the disk midplane, where the strong signal observed in the inner observations appears to be weaker in the outer observations (Fig. A.2). A similar Fe I flux deficit of

30−40% in the outer observations is evident in a comparison with UVES data, but the situation seems to be reversed in the Ca II H- and K emission, where the FLAMES fluxes at 60 AU are ∼1.5 times higher than corresponding UVES fluxes, while the data at 120 AU match fairly well (considering estimated errors for the Ca II extraction in that region). A cross-check of the flux-calibrated science spectra with the available HARPS spectrum of $\beta$ Pic allowed us to confirm that the slope of the fitted response curves is correct to within a few percent, therefore any relative differences between the strength of the Fe I and Ca II emission compared to UVES data is not caused by errors in the fit. Although the error bars assigned to UVES data indicate well-determined fluxes, similar difficulties in determining absolute photometric fluxes exist for that instrument, therefore any calibration of our data with respect to UVES data was not performed. Instead, we assumed that photometric errors and a higher seeing during the outer observations are likely to blame for the observed flux disagreements, and do not affect the qualitative results derived from our modelling (in which relative inner/outer discrepancies are also effectively averaged out).

## References


Ahmic, M., Croll, B., & Artymowicz, P. 2009, ApJ, 705, 529
Aitken, D. K., Moore, T. J. T., Roche, P. F., Smith, C. H., & Wright, C. M. 1993, MNRAS, 265, L41
Artymowicz, P. 1997, Ann. Rev. Earth Planet. Sci., 25, 175
Aumann, H. H. 1985, PASP, 97, 885
Backman, D. E., & Paresce, F. 1993, in Protostars and Planets III, eds. E. H. Levy, & J. I. Lunine, 1253
Beust, H., & Valiron, P. 2007, A&A, 466, 201
Beust, H., Vidal-Madjar, A., Ferlet, R., & Lagrange-Henri, A. M. 1990, A&A, 236, 202
Brandeker, A. 2011, ApJ, 729, 122
Brandeker, A., Liseau, R., Olofsson, G., & Fridlund, M. 2004, A&A, 413, 681
Brandeker, A., Olofsson, G., Vandenbussche, B., et al. 2012, A&A, submitted
Chen, C. H., & Jura, M. 2003, ApJ, 582, 443
Chen, C. H., Li, A., Bohac, C., et al. 2007, ApJ, 666, 466
Crawford, I. A., Spyromilio, J., Barlow, M. J., Diego, F., & Lagrange, A. M. 1994, MNRAS, 266, L65
Czechowski, A., & Mann, I. 2007, ApJ, 660, 1541
Dent, W. R. F., Walker, H. J., Holland, W. S., & Greaves, J. S. 2000, MNRAS, 314, 702
Dominik, C., & Decin, G. 2003, ApJ, 598, 626
Fernández, R., Brandeker, A., & Wu, Y. 2006, ApJ, 643, 509
Gorti, U., & Hollenbach, D. 2009, ApJ, 690, 1539
Grevesse, N., & Sauval, A. J. 1998, Space Sci. Rev., 85, 161
Grigorieva, A., Thébault, P., Artymowicz, P., & Brandeker, A. 2007, A&A, 475, 755
Haisch, Jr., K. E., Lada, E. A., & Lada, C. J. 2001, ApJ, 553, L153
Henning, T. 2010, ARA&A, 48, 21
Herczeg, G. J., Linsky, J. L., Walter, F. M., Gahm, G. F., & Johns-Krull, C. M. 2006, ApJS, 165, 256
Hobbs, L. M., Vidal-Madjar, A., Ferlet, R., Albert, C. E., & Gry, C. 1985, ApJ, 293, L29
Holland, W. S., Greaves, J. S., Zuckerman, B., et al. 1998, Nature, 392, 788
Jayawardhana, R., Coffey, J., Scholz, A., Brandeker, A., & van Kerkwijk, M. H. 2006, ApJ, 648, 1206
Kamp, I., & Bertoldi, F. 2000, A&A, 353, 276
Knacke, R. F., Fajardo-Acosta, S. B., Telesco, C. M., et al. 1993, ApJ, 418, 440
Krivov, A. V., Herrmann, F., Brandeker, A., & Thébault, P. 2009, A&A, 507, 1503
Lagrange, A.-M., Beust, H., Mouillet, D., et al. 1998, A&A, 330, 1091
Lagrange, A.-M., Backman, D. E., & Artymowicz, P. 2000, Protostars and Planets IV, 639
Lagrange-Henri, A. M., Vidal-Madjar, A., & Ferlet, R. 1988, A&A, 190, 275
Lecavelier Des Etangs, A., Vidal-Madjar, A., & Ferlet, R. 1996, A&A, 307, 542
Lecavelier Des Etangs, A., Vidal-Madjar, A., & Ferlet, R. 1998, A&A, 339, 477
Liseau, R., Brandeker, A., Fridlund, M., et al. 2003, A&A, 402, 183
Lovelace, R. V. E., Romanova, M. M., & Barnard, A. W. 2008, MNRAS, 389, 1233
Lynden-Bell, D., & Pringle, J. E. 1974, MNRAS, 168, 603
Moór, A., Ábrahám, P., Juhász, A., et al. 2011, ApJ, 740, L7
Najita, J., Carr, J. S., & Mathieu, R. D. 2003, ApJ, 589, 931
Nilsson, R., Liseau, R., Brandeker, A., et al. 2009, A&A, 508, 1057
Okamoto, Y. K., Kataza, H., Honda, M., et al. 2004, Nature, 431, 660
Olofsson, G., Liseau, R., & Brandeker, A. 2001, ApJ, 563, L77
Paresce, F., & Burrows, C. 1987, ApJ, 319, L23
Pascucci, I., Gorti, U., Hollenbach, D., et al. 2006, ApJ, 651, 1177
Redfield, S. 2007, ApJ, 656, L97
Roberge, A., & Weinberger, A. J. 2008, ApJ, 676, 509
Roberge, A., Feldman, P. D., Weinberger, A. J., Deleuil, M., & Bouret, J. 2006, Nature, 441, 724
Smith, B. A., & Terrile, R. J. 1984, Science, 226, 1421
Telesco, C. M., & Knacke, R. F. 1991, ApJ, 372, L29
Thébault, P., & Augereau, J.-C. 2005, A&A, 437, 141
Unno, W. 1952, PASJ, 4, 100
Vidal-Madjar, A., Ferlet, R., Hobbs, L. M., Gry, C., & Albert, C. E. 1986, A&A, 167, 325
Vidal-Madjar, A., Lagrange-Henri, A.-M., Feldman, P. D., et al. 1994, A&A, 290, 245
Weinberger, A. J., Becklin, E. E., & Zuckerman, B. 2003, ApJ, 584, L33
Wyatt, M. C., Smith, R., Su, K. Y. L., et al. 2007, ApJ, 663, 365
Xie, J.-W., Brandeker, A., & Wu, Y. 2012, ApJ, submitted [arXiv:1204.4087]
Zagorovsky, K., Brandeker, A., & Wu, Y. 2010, ApJ, 720, 923
Zuckerman, B. 2001, ARA&A, 39, 549
Zuckerman, B., & Becklin, E. E. 1993, ApJ, 414, 793
Zuckerman, B., Kim, S. S., & Liu, T. 1995, ApJ, 446, L79